

# A Distributed Massive MIMO Channel Sounder for “Big CSI Data”-driven Machine Learning

Florian Euchner, Marc Gauger, Sebastian Dörner, Stephan ten Brink  
Institute of Telecommunications, Pfaffenwaldring 47, University of Stuttgart, 70569 Stuttgart, Germany  
{euchner,gauger,doerner,tenbrink}@inue.uni-stuttgart.de

**Abstract**—A distributed massive multiple-input multiple-output (MIMO) channel sounder for acquiring large channel state information (CSI) datasets, dubbed **Distributed Channel Sounder by University of Stuttgart (DICHASUS)**, is presented. The measured data has potential applications in the study of various machine learning algorithms for user localization, Joint Communication and Sensing (JCAS), channel charting, enabling massive MIMO in frequency division duplex (FDD) operation, and many others. The proposed channel sounder architecture is distinct from similar previous designs in that each individual single-antenna receiver is completely autonomous, enabling arbitrary, spatially distributed antenna deployments, and offering virtually unlimited scalability in the number of antennas. Optionally, extracted channel coefficient vectors can be tagged with ground truth position data, obtained either through a global navigation satellite system (GNSS) receiver (for outdoor operation) or through various indoor positioning techniques.

## I. INTRODUCTION

To study massive multiple-input multiple-output (MIMO) channels, accurate wireless channel measurements from a multitude of receive antennas are required. Such channel measurements, referred to as channel state information (CSI), are acquired through a process known as channel sounding. Ever since the concept of massive MIMO was first introduced, the scientific community has placed significant effort into obtaining reliable and large CSI datasets. Early massive MIMO channel sounding experiments have been carried out since 2012 [1] [2] [3], followed by many more advanced channel sounders developed by different research groups in the subsequent years [4] [5] [6]. Nowadays, real-time massive MIMO testbeds have become commercially available [7] [8] [9], albeit at a rather expensive price point. More recently, an open source initiative for massive MIMO development, with a channel sounder based on hardware components from Skylark Wireless [9], was launched by a research group at Rice University [10]. All of these channel sounders, including a previous channel sounder developed at our institute [11], are primarily targeted at centralized massive MIMO deployments where all receivers are concentrated in a single antenna array.

While the idea of cell-less wireless networks is not new, in combination with massive MIMO, the concept has seen a surge in research interest over the last years. Research results, though only of theoretical nature, suggest that cell-less massive MIMO, also known as distributed massive MIMO, has advantages over network architectures based on small cells [12]. One objective of our channel sounder, **Distributed**

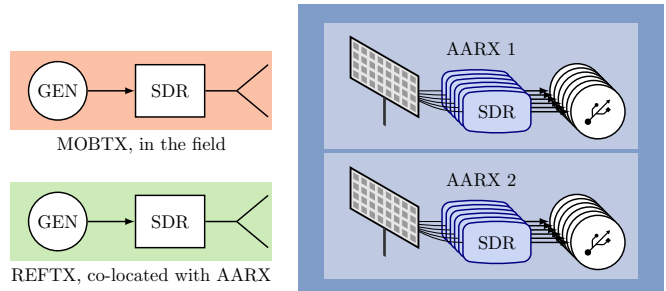


Fig. 1. Massive MIMO system set-up with single-antenna, mobile transmitter (MOBTX), reference transmitter (REFTX) and one or multiple individual antennas or antenna arrays with receivers (AARX) and USB flash storage.

**Channel Sounder by University of Stuttgart (DICHASUS)**, is to facilitate research into various distributed antenna deployment schemes, such as extremely large aperture arrays (ELAAs), where antennas are distributed along building facades or embedded into building structures as holographic antennas, as well as truly distributed antenna deployments across multiple buildings.

Therefore, DICHASUS was designed with a decentralized system architecture in mind: Rather than collecting all measurements at a central node, each receiver acquires and stores the samples from each antenna autonomously while staying tightly synchronized to a reference signal transmitter. This over-the-air synchronization method not only provides the flexibility to build distributed setups, but also enables straightforward scalability in the number of antennas and reduces overall system set-up complexity, which allows for rapid deployments of the channel sounder. A breakdown of the system architecture and a simple verification experiment are presented in Sections II through VI.

Captured DICHASUS datasets, one of which is described in Section VII, are made freely available to the scientific community<sup>1</sup>. In addition to the acquired CSI, we provide accurate labels such as position tags. In Section VIII, we demonstrate one possible application of the captured CSI data, namely neural network (NN)-based localization.

<sup>1</sup>Datasets, tutorials and sample code can be downloaded from <https://dichasus.inue.uni-stuttgart.de>.

## II. OVERALL SYSTEM SET-UP

DICHASUS covers the frequency range from 70 MHz to 6 GHz and every receiver has an analog to digital converter (ADC) bit depth of 12 bit. As depicted in Fig. 1, it consists of

- a) one or several groups of antenna arrays (AARX) as receivers, mimicking distributed base stations, described in detail in Section III,
- b) a reference transmitter (REFTX) for frequency, phase and timing calibration, at a location that ensures a low-attenuation propagation path to all AARX antennas, explained in Section IV and
- c) a mobile transmitter (MOBTX) with one transmit antenna in the field, which resembles a user equipment (UE), described in Section V.

The MOBTX continuously transmits cyclic prefix (CP)-orthogonal frequency division multiplex (OFDM)-modulated pilot symbols with a configurable number of subcarriers  $N_{\text{sub,mob}}$  and a maximal bandwidth of 50 MHz, enabling the extraction of CSI per subcarrier at the receiver antenna array. Also, the transmitter can embed its position, e.g., global navigation satellite system (GNSS) coordinates, into the transmit signal, making it possible to obtain CSI data together with position tags, which can later be used for supervised machine learning. The REFTX is placed in such a way that there is a good propagation path to each AARX receive antenna, e.g., a direct line-of-sight path. It also transmits CP-OFDM-based pilot signals with  $N_{\text{sub,ref}} = 128$  subcarriers at a bandwidth of 2 MHz, but in a different, non-overlapping frequency range, that is, MOBTX and REFTX are frequency-multiplexed. At all times, the AARX can receive both the signal from the MOBTX (through the channel of interest) as well as the signal from the REFTX. The individual single-antenna AARX receivers operate in an autonomous fashion, i.e., without a central clock, but with clock signals that are purely derived from each receiver's built-in crystal oscillator. Therefore, they rely on regular over-the-air frequency, phase and timing calibration using the REFTX's transmit signal, called REFTX broadcast. While the REFTX frequency may be inaccurate in absolute terms due to its own oscillator drift, by synchronizing every receiver to the same frequency reference, the relative offsets between receivers disappear.

## III. MASSIVE MIMO RECEIVER (AARX)

The AARX, shown in Fig. 2, is entirely built from comparably inexpensive commercial off-the-shelf (COTS) hardware components. Central to the AARX are Analog Devices' ADALM-PLUTO software-defined radios (SDRs) [13] that capture raw I/Q samples in a configurable frequency band received by the antennas. Each ADALM-PLUTO contains a Cortex-A9 microprocessor running a Linux-based firmware, on top of which a custom application is responsible for managing the sample capture. This way, all real-time signal processing functions can be performed by the receiver itself. Captured I/Q data is first transferred to the device's RAM,

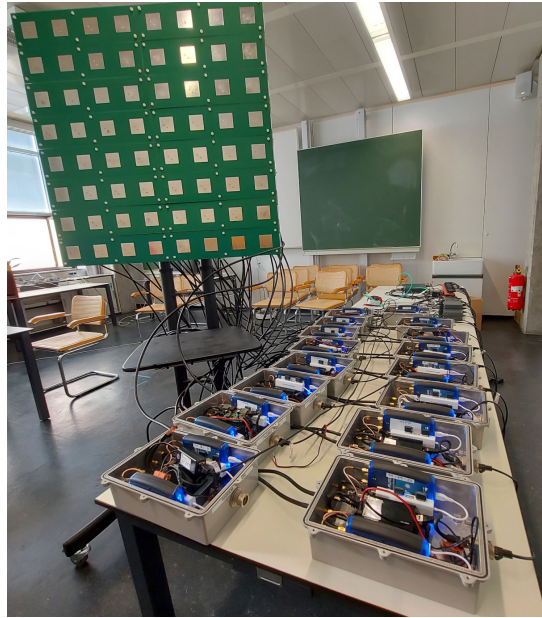


Fig. 2. Photo of 64-antenna AARX array (only 32 antennas of which are connected) on the left and autonomous AARX receivers on the right.

where 200 MB per device are allocated for sample buffering, and later stored onto one or multiple USB storage devices attached to each ADALM-PLUTO. While each ADALM-PLUTO is capable of capturing samples with a bandwidth of over 50 MHz to RAM, tests with typical USB storage devices show that a continuous writing speed of up to  $15 \text{ MB/s}$  is realistic. Real-time 12-bit I/Q sample capture is hence possible for capture rates of up to approximately 5 MHz. By, instead, only capturing short bursts, i.e., operating with a certain duty cycle, higher bandwidths are achievable. For example, even for a capture bandwidth of 50 MHz, the RAM buffer can hold more than one second of continuous I/Q samples.

All receivers are managed by a central controller, connected through Ethernet. The central controller does not perform any signal processing, but provides a graphical user interface through which all parameters of the data capture can be configured. Once the process of automatic calibration and capturing has been started, however, individual receivers can operate autonomously thanks to the reference transmitter (REFTX) concept, making this architecture easily scalable in the number of deployed AARX elements. In fact, since receivers store data in a decentralized fashion on their own USB flash storage devices, there is no need for high-speed networking for collecting data at a central node. During the channel sounding operation, the user interface on the central controller can be used for monitoring system parameters such as each antenna's signal-to-noise-ratio (SNR), buffer state or storage write speed.

Within one measurement campaign, all recordings are performed with fixed gain configurations at all transmitters and receivers so that channel attenuations are comparable between measurements at different points in time and space, i.e., automatic gain control (AGC) is disabled.

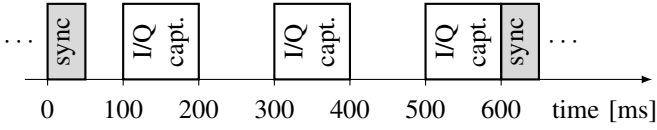


Fig. 3. Typical frequency / timing synchronization and I/Q sample capture burst schedule

#### IV. REFTX AND CHANNEL MODEL

With DICHASUS, multiple receivers can be deployed in a spatially distributed manner as long as reception of the REFTX broadcast signal is ensured. The REFTX signal is used for synchronization both in *real time* and later in an *off-line* postprocessing step, compare Fig. 4. In real time, the REFTX broadcast is used for two aspects of synchronization:

- Timing synchronization: The receivers typically do not record continuously, but in bursts, following a predefined schedule such as the one shown in Fig. 3. All receivers align this schedule to the received REFTX broadcast in time, with an accuracy that corresponds to the duration of one I/Q sample.
- Frequency synchronization: Each receiver's sampling and local oscillator clock are derived from an internal crystal oscillator through a phase locked loop (PLL). By adjusting the PLL's fractional- $n$  divider, local oscillator and sampling clock frequencies are synchronized with the REFTX down to approximately 0.025ppm.

Compared to off-line frequency correction, real time carrier frequency offset (CFO) and sampling frequency offset (SFO) correction has the advantage that SFO, the correction of which in digital processing is computationally expensive, becomes negligible over the short capture burst duration. The subsequent off-line postprocessing step improves synchronization by performing even more timing offset corrections, namely:

- CFO correction down to significantly less than 0.025ppm
- Phase correction so that the local oscillators of all receivers after correction can be considered to be phase-synchronous, except for the phase shift of the mostly flat channel between REFTX and receiver.
- Sub-sample sampling time offset (STO) correction so that the sampling instances can be considered to be identical across all receivers, except for the delay of the channel between REFTX and receiver.

This off-line synchronization is only possible due to the fact that the AARX receivers capture and store raw I/Q samples for the complete capture bandwidth, i.e., containing both REFTX and MOBTX signals.

The channels between REFTX antenna and the  $M$  AARX antenna elements may not all be perfectly identical, which is important to consider when performing STO and phase correction based on the REFTX broadcast. In a distributed setup, individual antennas may be separated by distances of several meters or more. Even under perfect line-of-sight conditions without scatterers, if the REFTX is not located at an equal distance to all AARX antenna elements, the different distances

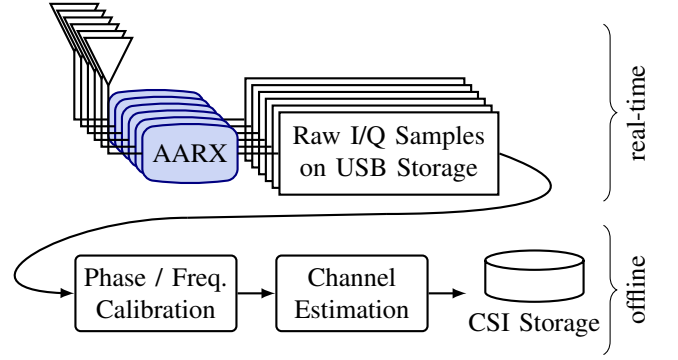


Fig. 4. Massive MIMO receiver architecture: Distributed sampling and raw data storage, centralized synchronization and analysis.

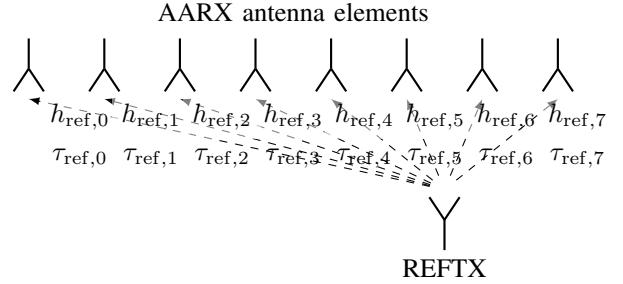


Fig. 5. Illustration of different-length line-of-sight channels between REFTX and AARX array antenna elements for  $M = 8$  AARX antennas.

between REFTX antenna and AARX antenna elements will lead to a fixed delay  $\tau_{\text{ref},m}$ , phase shift and path loss in the received signal specific to antenna  $m$  as illustrated in Fig. 5. After STO correction, which removes the effect of  $\tau_{\text{ref},m}$ , the channel experienced by a single subcarrier is approximately frequency-flat. For subcarrier  $i$ , its effect is described only by a channel coefficient  $h_{\text{ref},m,i} \in \mathbb{C}$ . With transmitted and received symbols  $s_{\text{ref},i}(k) \in \mathbb{C}$  and  $r_{\text{ref},m,i}(k) \in \mathbb{C}$  for subcarrier  $i$  at time instance  $k$ , our channel model is

$$r_{\text{ref},m,i}(k) = h_{\text{ref},m,i} s_{\text{ref},i}(k). \quad (1)$$

For all antenna elements and subcarriers, the value of  $h_{\text{ref},m,i}$  is unknown but assumed to be constant over time  $k$ . In practice, this is ensured by keeping REFTX and AARX at static positions and making sure that the propagation environment does not change. Due to the small REFTX bandwidth of 2 MHz and due to the strong propagation path between REFTX and each AARX antenna, the channel can be assumed to be approximately flat over all subcarriers, i.e., we assume

$$h_{\text{ref},m} \approx h_{\text{ref},m,i} \text{ for all } i = 0, \dots, N_{\text{sub,ref}} - 1. \quad (2)$$

#### V. MOBTX AND CHANNEL COEFFICIENT EXTRACTION

The channels between MOBTX and each AARX antenna fluctuate as the MOBTX moves in the field. For the channel between MOBTX and each AARX receive antenna, we use a channel model similar to the one in Eq. 1, except that the channel coefficients are no longer constant, but dependent on time index  $k$ :

$$r_{\text{mob},m,i}(k) = h_{\text{mob},m,i}(k) s_{\text{mob},i}(k) \quad (3)$$

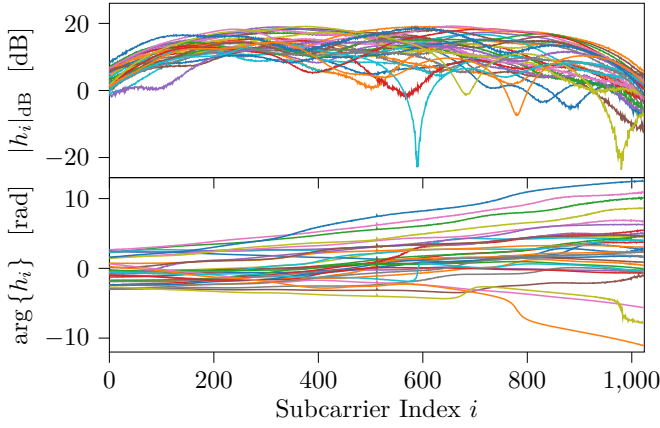


Fig. 6. Exemplary channel coefficient vectors for an indoor, mostly line of sight-channel with a few clearly visible notches. Each color represents one of the 32 AARX receive antennas. 1024 subcarriers are equally spaced over a bandwidth of 50 MHz.

In Eq. 3,  $s_{\text{mob},i}(k)$  denotes the symbol transmitted by the MOBTX at time instance  $k$  on subcarrier  $i$ ,  $r_{\text{mob},m,i}(k)$  denotes the corresponding received symbol for the AARX antenna with index  $m$  and  $h_{\text{mob},m,i}(k)$  is the time-dependent channel coefficient. After the sampled received baseband signals for each antenna have been synchronized in time, frequency and phase during postprocessing, subcarrier-specific channel coefficients  $h_{\text{mob},m,i}(k)$  can be extracted in another off-line processing step. To this end, a perfect reconstruction of the MOBTX transmit signal is produced. This is achieved by performing a maximal-ratio combining of the MOBTX receive signal of all antennas and then demodulating it. Through the use of error correction codes and checksums, the received symbols on all OFDM subcarriers, even those that are not pilots, can be traced back to their ideal constellation points. The effect of the channel is then computed based on Eq. 3 with known  $r_{\text{mob},m,i}(k)$  and  $s_{\text{mob},i}(k)$ , for all antennas and all subcarriers. If the duration of each OFDM symbol is much shorter than the channel coherence interval, multiple channel coefficient vectors within the same coherence interval that are captured within the same burst may be averaged to improve the SNR. The extracted CSI for a single coherence interval, referred to as a *datapoint*, is tagged with a timestamp and possibly some additional labels such as the position of the MOBTX. As illustrated in Fig. 6, the CSI for a particular time instance consists of multiple vectors of channel coefficients, one per AARX receive antenna. For the  $m^{\text{th}}$  receive antenna, the channel coefficient vector is given by  $\mathbf{h}_{\text{mob},m} \in \mathbb{C}^{N_{\text{sub},\text{mob}}}$ , where the  $i^{\text{th}}$  entry,  $h_{\text{mob},m,i}$ , contains the estimated channel coefficient for the MOBTX subcarrier with index  $i$ .

The use of a reference transmitter instead of distributing clock signals has important ramifications on the interpretation of the extracted channel coefficient phases: All receivers are synchronized in time and phase to their received REFTX broadcast, but, due to the different channels between REFTX and each AARX antenna as expressed in Eq. 1, they are not necessarily synchronous in absolute terms, i.e., in phase and sampling instances. The REFTX channel's phase shift leads

to a constant, antenna-specific phase rotation. Moreover, the different propagation path delays between REFTX and AARX antennas lead to a receiver-specific STO, which manifests itself as a subcarrier-dependent phase shift that increases or decreases linearly over the subcarrier frequency.

However, by ensuring the propagation environment between REFTX and AARX is static, all phase rotations remain constant and can be accounted for or even be removed through calibration. In many applications, including precoding for massive MIMO and CSI-fingerprinting-based positioning, phase differences between antennas that are accurate in absolute terms are not even required, as long as they are correct in relative terms. That is, phase offsets of individual antennas and subcarriers caused by the REFTX propagation path need to be constant over time and irrespective of the MOBTX position, which is the case.

We denote the REFTX-adjusted channel coefficient vector between MOBTX and AARX antenna  $m$ , i.e., the true channel coefficients that are unaffected by the channel between REFTX and AARX, by  $\mathbf{a}_{\text{mob},m}$ . Neglecting the propagation delay, the channel between REFTX and AARX antenna  $m$  is described by a single channel coefficient  $h_{\text{ref},m}$  (compare Eq. 2), which only leads to a constant phase rotation. If  $h_{\text{ref},m}$  is known, the adjusted MOBTX channel coefficient vector  $\mathbf{a}_{\text{mob},m}$  can be computed as

$$\mathbf{a}_{\text{mob},m} = \mathbf{h}_{\text{mob},m} e^{j \arg\{h_{\text{ref},m}\}} \text{ for } \tau_{\text{ref},m} \approx 0. \quad (4)$$

If, as is usually the case, the propagation path delays through the REFTX channel  $\tau_{\text{ref},m}$  are not negligible, the effect of a constant STO relative to other AARX receivers also has to be accounted for. For small STO values and narrow subcarrier spacing  $\Delta f_{\text{sub},\text{mob}}$ , if  $\tau_{\text{ref},m}$  is known, the effect of STO can be accounted for by undoing the phase shift it causes to subcarrier  $i$  with  $i = 0, \dots, N_{\text{sub},\text{mob}} - 1$ :

$$a_{\text{mob},m,i} = h_{\text{mob},m,i} e^{j(\arg\{h_{\text{ref},m}\} + 2\pi i \tau_{\text{ref},m} \Delta f_{\text{sub},\text{mob}})} \quad (5)$$

On the other hand, the amplitudes of the coefficients  $\mathbf{h}_{\text{mob},m}$  are not influenced by the REFTX propagation path, because measuring them does not require timing synchronization. In our datasets, all channel coefficient amplitudes are provided relative to an arbitrary, but constant reference amplitude level that is specific to each measurement campaign.

## VI. VERIFICATION: PHASE STABILITY

We carried out a set of experiments to verify that the proposed and implemented system architecture provides accurate and repeatable measurement results. One particularly insightful experiment demonstrates long-term phase stability and repeatability of CSI measurements. For this experiment, a MOBTX center frequency of 1.27 GHz with a bandwidth of 8 MHz and  $N_{\text{sub},\text{mob}} = 1024$  subcarriers was chosen and the REFTX operated at 1.262 GHz.

For a small-scale indoor test setup, the delay spread between multiple propagation paths is very small and the path delay between MOBTX and  $m^{\text{th}}$  AARX antenna element is assumed to only lead to a phase shift. According to the channel model

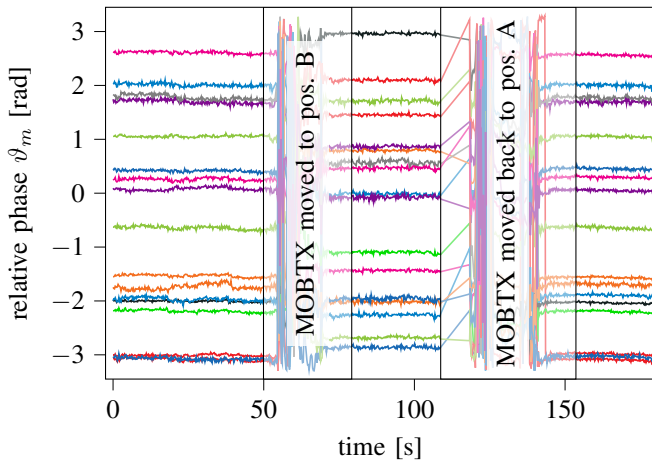


Fig. 7. Relative phases  $\vartheta_0, \dots, \vartheta_{16}$  from 17 (out of 32) antennas as measured in the experiment, plotted over time, verifying stability and spatial consistency. The other 15 antennas exhibited similar behavior and are only omitted as to not overload the diagram with too many colors.

given in Eq. 3, this phase shift is dependent on the subcarrier index  $i$ . For illustration purposes, we averaged the phases of all subcarriers, resulting in an average phase shift  $\vartheta_m(k)$  perceived by the  $m^{\text{th}}$  antenna at time index  $k$ , given by

$$\vartheta_m(k) = \arg \left\{ \sum_{i=0}^{N_{\text{sub,mob}}-1} h_{\text{mob},m,i}(k) \right\}. \quad (6)$$

The measured average phases  $\vartheta_m(k)$  of 17 out of 32 antennas, as a function of time elapsed since the start of the experiment, are shown in Fig. 7. In the beginning of the experiment, the MOBTX together with the REFTX and a single, concentrated 32-antenna array as AARX were placed in a static environment (a seminar room). The initial MOBTX placement is referred to as *Position A*. Channel measurements are acquired continuously throughout the experiment. After 50s of waiting, the MOBTX is moved to a different position in the same room, referred to as *Position B*. In Fig. 7, the change in received MOBTX phases is clearly visible. After approximately 30s at this new position, the MOBTX is returned to its original location, Position A. As can be observed from Fig. 7, all phases return to their original value, illustrating repeatability and spatial consistency of the set-up.

## VII. DATASET DESCRIPTION

At the point of writing, several datasets, measured in both indoor and outdoor environments, have been collected using DICHASUS. As an example that conveys what a typical dataset looks like, some characteristics of one particular indoor dataset will be outlined in the following. This dataset, called *dichasus-015x*, was collected using a robot, on top of which the MOBTX was mounted. The robot was programmed to drive along a meandering path inside certain areas of the room, while CSI was acquired by the AARX. This procedure was repeated multiple times, resulting in CSI datasets for multiple *round trips* of the robot, with a duration of 10 to

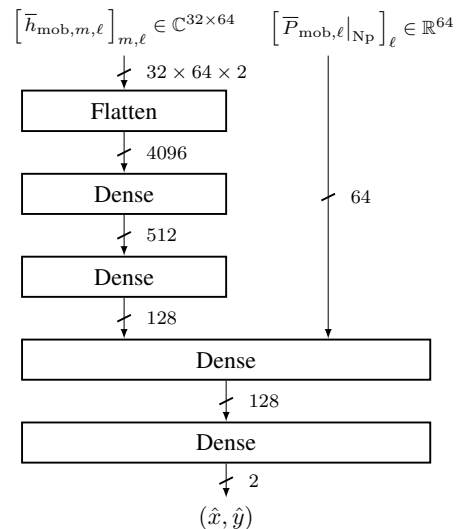


Fig. 8. Architecture of the NN used for CSI-based MOBTX localization.

20 minutes each. Channel coefficients from  $N_{\text{sub,mob}} = 1024$  subcarriers, spanning a bandwidth of 50 MHz, were acquired. In total, CSI was collected over a duration of 5467s amounting to 77607 datapoints or 20.4 GB of uncompressed, single precision complex floating point numbers. On average, more than 14 datapoints were collected per second with each datapoint containing channel coefficients averaged over complete capture bursts containing 90 MOBTX symbols. In addition to the channel coefficients, each datapoint is tagged with two MOBTX antenna position labels, one derived from a LiDAR that is part of the robot and one generated by a tachymeter tracking the antenna, as well as a timestamp, SNR and CFO information.

## VIII. VERIFICATION: NN-BASED POSITIONING

In another experiment, we verified that CSI and ground truth labels are suitable for a practical application based on CSI data, namely CSI-based positioning using NNs. We apply multiple robot round trips of aforementioned *dichasus-015x* dataset to this task. As a network architecture, the simple NN with four dense layers shown in Fig. 8 is used. We do not provide the channel coefficients for all 1024 subcarriers directly to the network, but only features derived from them, which are computed in a feature extraction stage. These features are:

- Mean normalized channel coefficients: For each antenna  $m = 0, \dots, M-1$ , the channel coefficients of  $p$  adjacent subcarriers are summed and then normalized over all antennas  $n = 0, \dots, M-1$ . We obtain averaged, normalized channel coefficients with  $\ell = 0, \dots, N_{\text{sub,mob}}/p - 1$ :

$$\bar{h}_{\text{mob},m,\ell} = \frac{\sum_{i=p\ell}^{p\ell+p-1} h_{\text{mob},m,i}}{\sqrt{\sum_{n=0}^{M-1} \left| \sum_{i=p\ell}^{p\ell+p-1} h_{\text{mob},n,i} \right|^2}} \quad (7)$$

The normalization ensures that  $\sum_{m=0}^{M-1} |\bar{h}_{\text{mob},m,\ell}|^2 = 1 \forall \ell$ . As the numeric values of channel coefficients

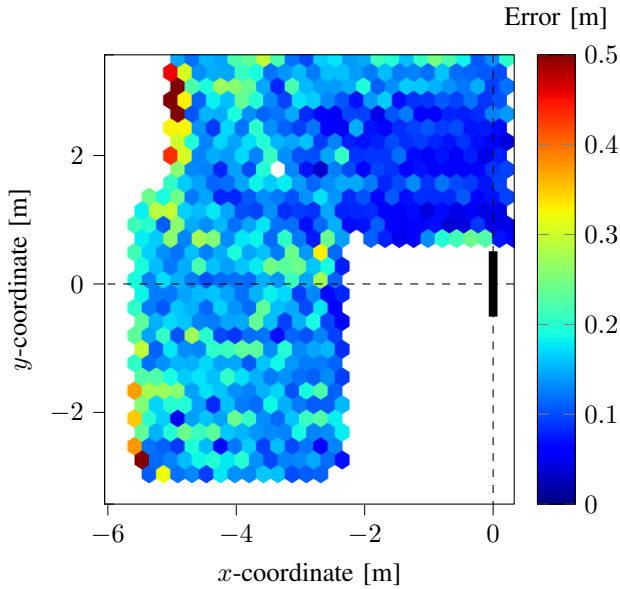


Fig. 9. Absolute localization error for an exemplary dataset with concentrated AARX antenna array (black rectangle) at position  $(x, y) = (0, 0)$ .

span several orders of magnitude for typical radio environments, this input normalization greatly improves NN performance.

- Subcarrier powers: The mean power over all antennas of the averaged channel coefficients before the normalization in Eq. 7 in logarithmic units:

$$\bar{P}_{\text{mob},\ell}|_{N_p} = \ln \left( \sum_{m=0}^{M-1} \left| \sum_{i=p\ell}^{p\ell+p-1} h_{\text{mob},m,i} \right|^2 \right)$$

The intention of providing these power values is to give the network an indication of the distance between MOBTX and AARX.

We choose  $p = 16$ , yielding  $N_{\text{sub,mob}}/p = 64$  averaged normalized channel coefficients for our dataset with 1024 subcarriers. Since we provide the real and imaginary parts of  $\bar{h}_{\text{mob},m,\ell} \in \mathbb{C}$  for all  $M = 32$  antennas separately to the NN, the averaged normalized channel coefficient input tensor's dimensionality is  $M \times N_{\text{sub,mob}}/p \times 2$ .

Training is performed on a training set that contains all datapoints from two complete round trips, with batch sizes 32, 64, 256, 1024 and 4096 and 20 epochs per batch size. The trained network then estimates positions based on CSI from a third round trip, our test set. While the robot always stays inside the same part of the room during every round trip, it may drive along a different path, hence the visited locations from one round trip do not precisely match those from previous trips. By training and evaluating on different robot round trips, the network is presented inputs from positions in the room that it has never seen before during training. Fig. 9 illustrates the quality of the position estimates  $(\hat{x}, \hat{y})$  generated by the NN for the outlined scenario. Over the complete test set, we achieve a mean absolute error of less than 0.2 m.

## IX. SUMMARY AND OUTLOOK

The system architecture of a distributed massive MIMO channel sounder with over-the-air synchronization, suitable for researching cell-less massive MIMO systems and various antenna deployments, has been presented. To verify the suitability of our approach, first captured datasets have been generated and analyzed. The captured datasets can be used to tackle open research questions in a variety of domains and to empirically verify theoretical results.

Two particularly interesting applications are channel charting [14] and enabling massive MIMO in frequency division duplex (FDD) operation [15]. CSI captured by DICHASUS may be used to verify results previously only obtained through simulations with real-world measurement data.

## REFERENCES

- [1] X. Xie, E. Chai, X. Zhang, K. Sundaresan, A. Khojastepour, and S. Rangarajan, "Hekaton: Efficient and practical large-scale MIMO," in *Proceedings of the 21st Annual International Conference on Mobile Computing and Networking*, 2015, pp. 304–316.
- [2] C. Shepard, H. Yu, N. Anand, E. Li, T. Marzetta, R. Yang, and L. Zhong, "Argos: Practical many-antenna base stations," in *Proceedings of the 18th annual international conference on Mobile computing and networking*, 2012, pp. 53–64.
- [3] S. Malkowsky, J. Vieira, L. Liu, P. Harris, K. Nieman, N. Kundargi, I. C. Wong, F. Tufvesson, V. Öwall, and O. Edfors, "The world's first real-time testbed for massive MIMO: Design, implementation, and validation," *IEEE Access*, vol. 5, pp. 9073–9088, 2017.
- [4] P. Harris, W. B. Hasan, S. Malkowsky, J. Vieira, S. Zhang, M. Beach, L. Liu, E. Mellios, A. Nix, S. Armour *et al.*, "Serving 22 users in real-time with a 128-antenna massive MIMO testbed," in *2016 IEEE International Workshop on Signal Processing Systems (SiPS)*. IEEE, 2016, pp. 266–272.
- [5] J. Vieira, S. Malkowsky, K. Nieman, Z. Miers, N. Kundargi, L. Liu, I. Wong, V. Öwall, O. Edfors, and F. Tufvesson, "A flexible 100-antenna testbed for massive MIMO," in *2014 IEEE Globecom Workshops (GC Wkshps)*. IEEE, 2014, pp. 287–293.
- [6] X. Jiang, F. Kaltenberger, R. Knopp, and H. Maatallah, "OpenAirInterface massive MIMO testbed: A 5G innovation platform," in *Proceedings of the 21st International ITG Workshop Smart Antennas, Berlin, Germany*, 2017, pp. 15–17.
- [7] Nutaq. (2015) 5G Massive MIMO Testbed. [Online]. Available: <https://nutaq.com/5g-massive-mimo-testbed>
- [8] NI. What Is the MIMO Prototyping System? [Online]. Available: <https://www.ni.com/de-de/shop/wireless-design-test/what-is-the-mimo-prototyping-system.html>
- [9] Skylark wireless. [Online]. Available: <https://skylarkwireless.com/products/research/>
- [10] (2019) RENEW: Reconfigurable Eco-system for Next-generation End-to-end Wireless. [Online]. Available: <https://renew.rice.edu/>
- [11] M. Arnold, J. Hoydis, and S. ten Brink, "Novel massive MIMO channel sounding data applied to deep learning-based indoor positioning," in *SCC 2019; 12th International ITG Conference on Systems, Communications and Coding*. VDE, 2019, pp. 1–6.
- [12] H. Q. Ngo, A. Ashikhmin, H. Yang, E. G. Larsson, and T. L. Marzetta, "Cell-free massive MIMO versus small cells," *IEEE Transactions on Wireless Communications*, vol. 16, no. 3, pp. 1834–1850, 2017.
- [13] ADALM-PLUTO SDR Active Learning Module, Analog Devices. [Online]. Available: <https://www.analog.com/media/en/news-marketing-collateral/product-highlight/ADALM-PLUTO-Product-Highlight.pdf>
- [14] C. Studer, S. Medjkouh, E. Gönültaş, T. Goldstein, and O. Tirkkonen, "Channel Charting: Locating Users within the Radio Environment using Channel State Information," *CoRR*, vol. abs/1807.05247, 2018. [Online]. Available: <http://arxiv.org/abs/1807.05247>
- [15] M. Arnold, S. Dörner, S. Cammerer, S. Yan, J. Hoydis, and S. ten Brink, "Enabling FDD massive MIMO through deep learning-based channel prediction," *arXiv preprint arXiv:1901.03664*, 2019.